Supplementary Materials for

Light curves of the neutron star merger GW170817/SSS17a: Implications for r-process nucleosynthesis

M. R. Drout,* A. L. Piro, B. J. Shappee, C. D. Kilpatrick, J. D. Simon, C. Contreras, D. A. Coulter, R. J. Foley, M. R. Siebert, N. Morrell, K. Boutsia, F. Di Mille, T. W.-S. Holoien, D. Kasen, J. A. Kollmeier, B. F. Madore, A. J. Monson, A. Murguia-Berthier, Y.-C. Pan, J. X. Prochaska, E. Ramirez-Ruiz, A. Rest, C. Adams, K. Alatalo, E. Bañados, J. Baughman, T. C. Beers, R. A. Bernstein, T. Bitsakis, A. Campillay, T. T. Hansen, C. R. Higgs, A. P. Ji, G. Maravelias, J. L. Marshall, C. Moni Bidin, J. L. Prieto, K. C. Rasmussen, C. Rojas-Bravo, A. L. Strom, N. Ulloa, J. Vargas-González, Z. Wan, D. D. Whitten

*Corresponding author. Email: mdrout@carnegiescience.edu

Published 16 October 2017 on *Science* First Release
DOI: 10.1126/science.aaq0049

This PDF file includes:

Materials and Methods

S1 Data Acquisition & Reductions

Swope Supernovae Survey 17a (SSS17a) was discovered in an i-band image obtained with the 1-m Swope telescope at Las Campanas Observatory at UT 2017 August 17 23:33, 10.9 hours after the LIGO Scientific Collaboration and Virgo Collaboration (referred to jointly as LVC) gravitational wave trigger (*28, 29*). Immediately after discovery, we initiated a follow-up campaign of optical and near-IR photometric observations of SSS17a spanning from $\sim$11 hours to 18.5 days after the LVC trigger. In the sections below, we describe the data acquisition, reduction, and calibration. All photometry is presented in Table S1 on the AB magnitude scale.

S1.1 Swope Photometry and Field Star Calibration

Following the discovery of SSS17a, we obtained observations with the Swope telescope in the *BVgri* bands on five additional nights spanning 2017 August 18 to 2017 August 24. Details of the observations and data reduction are described in a companion paper (*29*) We performed all reductions of our Swope imaging using `photpipe` (*54, 55*) as described in (*29*). Panoramic Survey Telescope and Rapid Response System (PanSTARRS) magnitudes of stars in the field of SSS17a were transformed into the Swope natural system using Supercal transformations (*56*).

S1.2 Magellan/LDSS-3 and Magellan/IMACS Optical Imaging

Photometric observations of SSS17a post-discovery included a series of three, 30 s g-band images obtained with the LDSS-3 imaging spectrograph on the 6.5-m Magellan/Clay telescope (*29, 30*). Observations were obtained between UT 00:08 and 00:20 on 2017 August 18. These images served both as confirmation of the transient (*29*) and acquisition images for the spectra of SSS17a (*31, 32*).

On subsequent nights, we continued to observe SSS17a with LDSS-3 in the *Bgriz* bands. Observations were obtained on six additional nights spanning 2017 August 18 to 2017 August 25 and included z-band spectroscopic acquisition images and 2–5, 60 s exposures in the B- and g-bands, obtained once the transient had faded below the level accessible to the Swope telescope. In addition we observed SSS17a in the r-band on 2017 August 19 and the z-band on 2017 August 29 with the Inamori-Magellan Areal Camera and Spectrograph (IMACS; (*57*)) on the Magellan/Baade telescope.

Bias and flat field corrections were made to all LDSS-3 and IMACS images using standard routines in IRAF (*58*). For observations obtained within 3.5 days of the LVC trigger, all exposures were reduced independently. After that date, nightly stacks were produced in each band.

In order to account for host-galaxy light when performing photometry, we make use of the symmetry of the host galaxy. The galaxy light was subtracted after a 180 degree rotation around its center, thus flattening the target's background. Tests on several images using Pan-STARRS1 3π images (*59*) of the field as templates yield consistent photometry, but worse residuals near the galaxy core. After galaxy subtraction, point-spread function (PSF) photometry was performed on each image using IRAF `daophot` (*60*) tasks. Absolute calibration was performed using magnitudes of field stars. For observations in *Bgri*, we use field star magnitudes calibrated by the Swope telescope. For z-band observations, our magnitudes are tied directly to Pan-STARRS1 magnitudes (*61*). All magnitudes are listed in Table S1.

S1.3 Magellan/FourStar and du Pont/RetroCam near-IR Photometry

We observed SSS17a using the FourStar near-IR camera (*62*) mounted on the 6.5-m Magellan/Baade telescope and the RetroCam near-IR camera mounted on the 2.5-m du Pont telescope at Las Campanas Observatory. FourStar observations were obtained on 11 nights beginning

11.5 hours after the LVC trigger as part of a joint Swope-Magellan search (*29*). The observations span 2017 August 17 to 2017 September 7 (0.5 to 18.5 days post-LVC trigger) and were obtained in the $J1$ (approximately Y), J, H, and $K_{\rm s}$ filters. RetroCam observations were carried out over 6 nights between 2017 August 21 and 2017 August 27 (4.5 to 10.5 days post-LVC trigger) in Y, J and H. Initial FourStar and Retrocam data reduction was performed following normal procedures of dark subtraction and flat fielding. In addition, a linearity correction was applied to FourStar data and a fringing mask was subtracted from RetroCam images. Dithered pointing sequences were then co-added into final image combinations, masking bad pixels.

SSS17a remained bright in the near-IR for over three weeks after the LVC trigger, during which the target was only visible close to twilight. It was therefore not possible to obtain high-quality near-IR template images for image subtraction. In order to account for host galaxy light from NGC 4993 when measuring photometry of SSS17a, we again make use of the host galaxy symmetry, subtracting a 180 degree rotated image, as described above.

The instrumental PSF photometry was measured in most images using IRAF's `daophot` package (*60*). For some images with a low signal-to-noise ratio, an empirical PSF was measured on a bright star and fit via a Markov Chain Monte Carlo (MCMC) to the target and other stars in the field. In this case, a bright star in the image is selected, sky subtracted, subsampled, and then stored in a 2-dimensional array. This array is used as a model of the PSF, which is then fitted to the target and stars individually, using an MCMC procedure where the fitted variables are the amplitude and the center of the star.

The final photometry of the target is measured relative to the calibrated stars in the field. The absolute calibration of field stars was made on one photometric night (2017 August 21) on du Pont/RetroCam for the Y, J and H bands. $K_{\rm s}$-band calibration of field stars was tied to the Two Micron All Sky Survey (2MASS) catalog (*63*). Calibrations from 2MASS or du Pont/Retrocam are fully consistent for the J and H bands. Final photometry is presented

in Table S1 on the AB magnitude system. Instrumental magnitudes were converted to the AB scale using offsets from (*64*) for $K_{\rm s}$ and (*65*) for Y, J, and H.

The FourStar imaging of SSS17a obtained on the night of discovery used integration times long enough that the sky emission was saturated by the end of the exposure. However, the data saved by the detector electronics consist of the difference between the voltage of each pixel at the end of the exposure and the voltage after the 1.456 s it takes for an initial read of each pixel at the beginning of the exposure. A saturated image therefore contains a negative image of the field with an exposure time of 1.456 s. We reduced these data by subtracting a template of the saturation pattern and then taking the difference between consecutive dithered frames to remove any remaining sky emission or dark current. We combined the available dithered frames to construct a final image. We then made photometric measurements as described above.

S1.4 Swift Ultraviolet and Optical Photometry

We performed photometry on 9 epochs of publicly available *Swift* Ultraviolet/Optical Telescope (UVOT) observations of SSS17a taken between 2017 August 18 and 2017 August 21 (*66, 67*). The UVOT observations were obtained in 6 filters: v (effective wavelength 5402 Å), b (4328 Å), u (3494 Å), $uvw1$ (2589 Å), $uvm2$ (2228 Å), and $uvw2$ (2030 Å) (*68*). See S2.3 for discussion of the influence of the Swift-UVOT transmission functions on the analysis presented.

We extracted source counts from a 3.0″ radius region around the transient using the software task UVOTSOURCE. In order to account for host galaxy light, we extracted background counts from several 3.0″ radius regions at a similar distance from the host galaxy core. Count rates were converted into magnitudes and fluxes using the most recent UVOT calibrations (*68, 69*).

Our results produce UV and u-band magnitudes that are $\sim$0.1$-$0.2 mag fainter than the values reported in (*66*) and (*67*). The deviation is larger in redder bands, where the host galaxy is brighter, and we attribute this difference to our method of background subtraction. If we

instead choose a background region that is well separated from NGC 4993, we recover magnitudes consistent with those previously reported in the Gamma-ray Coordinates Network (GCN) circulars (*66, 67*). Applying the same methods described above to the *Swift* b and v band images shows evidence for continued galaxy contamination, in the form of a flat light curve with large uncertainties over a $\sim$2 day timespan, which conflicts with evolution seen in higher resolution ground-based (e.g LDSS-3) imaging at similar wavelengths. In this manuscript, we report only values from *Swift* u, $uvw1$, $uvm2$ and $uvw2$ bands. All measured values are reported in Table S1 on the AB scale.

S1.5 PESSTO EFOSC and SOFI Imaging

The Public ESO Spectroscopic Survey of Transient Objects (PESSTO) (*70*) obtained optical imaging of SSS17a with the ESO Faint Object Spectrograph and Camera v.2 (EFOSC2) (*71*) and near-IR imaging with Son OF ISAAC (SOFI) (*72*) on the New Technology Telescope (NTT) beginning on 2017 August 18 (*73*). We downloaded the raw PESSTO observations from the ESO archive and reduced them using the Pyraf pipeline described by (*70*). The PESSTO optical imaging consists of three 300 s exposures in U and several $10 - 60$ s exposures in V per night on the nights of 2017 August 18-19, 2017 August 19-20, and 2017 August 20-21. The PESSTO near-IR imaging consists of a sequence of $48 - 67$ dithered 90 s or 120 s exposures in a single band (J, H, or $K_{\rm s}$) per night.

We performed PSF photometry on the U- and V-band images using the `IRAF` task `daophot` and calibrated the instrumental magnitudes using stars in the Swope V- and *Swift* U-band images. Photometry on the SOFI J, H, and $K_{\rm s}$ images was carried out as described above for Magellan/FourStar.

S1.6 Keck Imaging

We imaged SSS17a with the Low Resolution Imaging Spectrometer (LRIS) (*74, 75*) on the Keck-I 10 m telescope on 24 August 2017 from UT 05:35 to 06:24. LRIS was configured in imaging mode with g and I filters on the blue and red sides, respectively, and the D560 dichroic. We observed SSS17a in 11 blue-side frames and 27 red-side frames starting during twilight, and our exposure times varied from 14–124 s on the blue side and 25–120 s on the red side. In order to minimize readout time on the red side, we binned the image 2×2 and read out only the central 4 arcmin $\times$ 4 arcmin region. Conditions were near photometric at the start of observations with $\sim$0.8$''$ seeing, although the seeing degraded significantly in exposures at higher airmasses. We obtained bias frames and sky flats in the same instrumental configuration and the Landolt standard star field SA95 275 (*76*) was observed at a similar airmass.

We reduced all Keck/LRIS images using the semi-automatic IDL/python software `LPipe` (*77*). Individual frames were bias corrected, flattened, and then registered using stars in the 2MASS Point Source Catalog (*63*). We aligned and co-added the registered images, weighting by the inverse variance of the emission-free regions. We performed PSF photometry using `daophot` (*60*) and calibrated our photometry using APASS and Landolt standard stars (*76, 78*) from our standard star field.

S1.7 Synthetic Photometry from Flux-Calibrated Spectra

In addition, we supplement the photometry measured from broad-band imaging described above with synthetic photometry performed on flux calibrated spectra of SSS17a. Full details of the spectroscopic observations, reductions, calibration and synthetic photometry are described in (*32*). Briefly, the final flux calibrated spectra were corrected for instrumental response, atmospheric dispersion, differential flux losses, and telluric absorption, and were then scaled to the broad-band photometry described above.

The full set of synthetic photometry measured from the spectral sequence of SSS17a between 0.5 and 4.5 days can be found in (*32*). In this manuscript, we supplement our existing light curves and SEDs with measurements from synthetic photometry under the following conditions: (1) they add to a band in which we had existing observations, (2) they were obtained from a high S/N spectrum, (3) the entire filter response function falls within the observed spectrum, and (4) the relevant band lies interior or adjacent to the broad-band photometric points used to scale the spectrum. This results in the addition of *V*, *r*, and *z*-band measurements from the first night of observations and individual *V* and *z*-band points on later epochs. Synthetic photometry used in this analysis is presented in Table S1.

S2 Photometric Analysis

S2.1 Distance and Reddening

SSS17a exploded in NGC 4993 at a distance of $\sim$40 Mpc. Throughout this manuscript we adopt the Tully-Fisher distance of 39.5 Mpc from (*79*).

We adopt a value of $E(B-V)$ = 0.106 for the color excess due to Milky Way reddening in the direction of SSS17a based on the dust maps of (*80*). $E(B-V) \equiv A_B - A_V$ where A_B and A_V are the total extinction in the B and V band, respectively. This value is consistent with estimates based on Milky Way Na D absorption lines observed in high resolution spectra of SSS17a (*32*). Photometry is corrected for this reddening using a Milky Way extinction curve from (*81*) with the parameter $R \equiv A_V/E(B-V) = 3.1$. We use the SED of the source to iteratively calculate the extinction in each filter, A_λ, at each epoch as described below. Throughout this manuscript, we do not correct for reddening due to dust within the host galaxy. The lack of observed Na D features at the redshift of NGC4993 favors a low intrinsic absorption (*32*).

S2.2 Basic Photometric Properties from the UV to near-IR

The full light curve of SSS17a from the UV through near-IR is shown in Figure 1. In Table S2 we provide several basic parameters derived from the photometry in each band.

The quoted peak apparent and absolute magnitudes are observed values. For bands blueward of z-band, which rise in less than 12 hours, these are lower limits to the true peak. SSS17a peaks between -15.5 and -16.0 mag (AB) from the optical to near-IR, similar to the faintest core-collapse supernovae. In Figure S1 we plot the *V*, *i*, and *H*-band absolute magnitude light curves of SSS17a—accounting for the distance to NGC4993 and Milky Way reddening. Also shown are the F160W (roughly rest-frame *H*-band) measurement and F6060W (roughly rest-frame *V*-band) upper limit for the tentative kilonova associated with short GRB 130603B (*23, 24*). At $+7$ days from the burst, GRB130603B has a slightly higher near-IR luminosity than observed for SSS17a.

In Table S2 we also report several measurements of the rise and decline timescales of SSS17a. We determine the time over which a band declines by half of its peak luminosity ($t_{1/2}$) and number of magnitudes the light curve decline in the first 5 days after maximum (ΔM_5) by linearly interpolating the observed light curves. A linear decline rate was also obtained by fitting the data between maximum light and +5.5 days. SSS17a declines at a rate ranging from 2.6 mag day^{-1} (u-band) to 0.1 mag day^{-1} (H-band). The observed optical light curves are generally consistent with a single slope post-maximum. However, our final B-band points indicate a shallowing of the decay rate between 5 and 10 days post-merger.

SSS17a peaks earlier and declines faster in bluer bands. As a result, its colors transition quickly to the red. Between +0.5 and +4.5 days the $V - H$ color of SSS17a evolves from -1.2 mag to 3.6 mag (top panel, Figure S1). By comparison, the late time emission from GRB130603B was attributed to a kilonova in part because of its red color ($V - H > 1.9$ mag).

The characteristic timescale of SSS17a is faster than other known transients. For example,

$t_{1/2} \sim 1.1$ days in r-band is nearly a factor of 5 smaller than the fastest rapidly-evolving and luminous transient discussed in (*82*). A detailed comparison of the properties of SSS17a to other transients is made in (*34*).

S2.3 SED and Bolometric Light Curve Construction

We construct SEDs for SSS17a from our observed photometry at 10 epochs using the iterative, forward-modeling approach described in (*83*). This approach aims to mitigate systematic errors that occur when constructing an SED from photometry by applying standard offsets to obtain fluxes at filter's pivot or effective wavelength. The translation from an observed broad-band magnitude to a flux at a given wavelength is fundamentally a function of the source's spectrum, and systematic errors can be particularly large when applying standard conversion factors to Swift-UVOT $uvw1$ and $uvw2$ observations of red sources (*83*).

We begin by interpolating our observed light curves to a set of common epochs. Our observations predominately come from Las Campanas Observatory and other telescopes in Chile, where SSS17a was only visible for the first $\sim$1 hour of the night. As a result our SEDs are constructed predominately on daily, evenly-spaced epochs between 0.5 and 8.5 days after the LVC trigger. In addition, we also compute compute SEDs at the 0.67 and 1.0 days. These correspond to the first two epochs of Swift UVOT data, when the transient was rapidly evolving.

With our photometry integrated to common epochs, we then construct a simple SED with "pivot" points at the effective wavelength of each observed band and the outer edge of the filter functions for the exterior bands. The flux level at each pivot point is then adjusted until synthetic photometry performed on this simple SED is consistent with the observed measurements. Extinction correction factors, A_λ, and flux conversion factors for each band are then computed from this best-fitting SED and applied to the original data.

The time evolution of the resulting SEDs is shown in Figure 3. In Figure S2 we plot each

epoch individually for clarity. As in Figure 3, the shaded bands represent best-fit blackbody temperatures for each epoch. For epochs 0.67 and 1.0 days, data redward of the Swift-u band data is derived from interpolating our ground based optical data on days 0.5 and 1.5. We find very similar best-fit blackbody temperatures if only the Swift-UVOT data are modeled.

SSS17a undergoes dramatic cooling over the first day post-merger. Between our first observations at 0.5 days, and the first epoch of *Swift*-UVOT measurements $\sim$ 4 hours later, we infer a total cooling of $\sim$2400K, or 600 K hr^{-1}. Evidence for this rapid cooling is also seen in the evolution of the continuum between spectra taken $\sim$ 1 hour apart on the first night of observations (*32*).

While the SEDs are generally consistent with a thermal distribution, there are a few exceptions. Between days 1.5 and 4.5 the Y-band measurements consistently lead to fluxes in excess of the best-fit blackbody distribution. This is consistent with the emergence of a feature in in the optical spectra around $\sim 1\mu$m at similar epochs (*32*). In addition, an apparent excess is visible in the g-band ($\sim$4800 Å) at similar epochs. These features are indicated by dotted lines in Figure S2. At late epochs ($>$ 5.5 days) the slope between the bluest observed bands are steeper than a thermal distribution, possibly indicative of line-blanketing.

Pseudo-bolometric luminosities at each epoch were constructed by integrating these best-fit SEDs after applying a Milky Way extinction curve, and corrected for missing flux as described in the main text. At 0.5 days post-merger SSS17a has a bolometric flux of $\sim 10^{42}$ erg s^{-1}.

S3 R-Process Heating and Ejecta Property Estimates

Models of r-process powered transients have become increasingly sophisticated over the last decade. Early models first showed that radioactive ejecta from a neutron star merger can power an electromagnetic transient, but assumed that the energy was provided by some fraction of the rest mass energy rather than using an actual model for the radioactive decay (*12*). The idea of

a macronova or kilonova was then re-popularized by newer models that invoked the decay of radioactive species, without making the connection to r-process nucleosynthesis (*13, 84*). The first true r-process powered transient calculation soon followed (*14*), and since that time the theoretical studies have quickly matured with more detailed nuclear networks, hydrodynamics in multi-dimensional numerical simulations, and detailed treatments of the radiative transfer. Here we summarize some of the basic aspects of r-process transients for use in comparing with our data. A more detailed comparison with specific models is provided in a companion paper (*44*).

One of the most robust predictions of r-process heating is the $t^{-1.3}$ dependence of the energy generation rate, $\dot{q}_r$ (*14, 15*). We fit the heating rate from these works to find

$$\dot{q}_r = 3 \times 10^{10} t_{\rm day}^{-1.3} \,{\rm erg\,s^{-1}\,g^{-1}}, \tag{S1}$$

where $t_{\rm day}$ is the time since explosion in units of days. There can be a ≈30% correction to this heating rate depending on Y_e. The thermalization depends on the ability to absorb the energy with energy losses from weak processes. To account for thermalization efficiency, $\epsilon_{\rm th}$, we use the fitting function

$$\epsilon_{\rm th} = 0.36 \left[\exp(-a t_{\rm day}) + \frac{\left(1 + 2bt^d\right)}{2bt_{\rm day}^d} \right], \tag{S2}$$

where a, b, and d are fitting parameters whose values depend on the mass of of r-process elements, $M_{\rm r}$ and the average (lowest) velocity in the ejecta, v_0. $a = 0.56$, $b = 0.17$, and $d = 0.74$ are appropriate for $M_{\rm r} = 0.1\,M_\odot$ and $v_0 = 0.1c$ (*85*). Combining the above expressions the total r-process luminosity is

$$L_r = \epsilon_{\rm th} \dot{q}_r M_r, \tag{S3}$$

The rise time to peak (t_p) for an optically thick transient is roughly set by when the diffusion time is equal to the expansion time for the ejecta (*35*). For ejecta with a velocity gradient $v = v_0 (M_v/M_r)^{-1/\beta}$, where M_v is the total mass with velocity greater than v, this timescale

can be approximated as

$$t_p \approx \left(\frac{\kappa M_r}{3\beta v_0 c}\right)^{1/2}, \tag{S4}$$

where κ is the specific opacity (*17*). A characteristic value for β motivated by numerical simulations is about 3 (*86, 87*), although in general the ejecta structure can be more complicated than in such simulations (*16*). Solving this equation for κ and requiring that $t_p \lesssim 0.5\,\mathrm{days}$, we find an upper limit to the opacity during the peak of the kilonova of $\kappa \approx 0.08\,\mathrm{cm^2\,g^{-1}}$.

Similarly, the optical depth of a given depth moving at velocity v is

$$\tau_v = \int_r^\infty \kappa \rho_v dr, \tag{S5}$$

where

$$\rho_v \approx \frac{3M_v}{4\pi(vt)^3} = \frac{3M_r}{4\pi(vt)^3}\left(\frac{v}{v_0}\right)^{-\beta} \tag{S6}$$

is roughly the density of the material moving at v. Performing this integral and evaluating it at $v = v_0$, we find that the total optical depth is

$$\tau = \frac{3\kappa M_r}{4\pi(1+\beta)t^2 v_0^2}. \tag{S7}$$

Solving for the time when $\tau \approx 1$

$$t_{\tau=1} \approx \left[\frac{3\kappa M_r}{4\pi(1+\beta)v_0^2}\right]^{1/2}, \tag{S8}$$

thus up to a factor of order unity $t_{\tau=1} \approx (c/v_0)^{1/2} t_p$. Setting $t_{\tau=1} \approx 20\,\mathrm{days}$ (motivated by the observed duration of the SSS17a emission), we derive a lower limit on the opacity of the red/cool component of $\kappa \gtrsim 5\,\mathrm{cm^2\,g^{-1}}$.

S4 Constraints on Radioactive Nickel Heating

Most hydrogen-deficient supernovae are powered by the radioactive decay of ^{56}Ni, but radioactive nickel heating cannot reproduce the entire photometric evolution of SSS17a. The heating

from the decay of ^{56}Ni and subsequently ^{56}Co, $\dot{q}_{56}$, scales as

$$\dot{q}_{56} = \dot{q}_{\rm Ni} \exp(-t/\tau_{\rm Ni}) + \dot{q}_{\rm Co}[\exp(-t/\tau_{\rm Co}) - \exp(-t/\tau_{\rm Ni})] \tag{S9}$$

where $\dot{q}_{\rm Ni} = 3.9 \times 10^{10}\,{\rm erg\,g^{-1}\,s^{-1}}$, $\dot{q}_{\rm Co} = 6.8 \times 10^{9}\,{\rm erg\,g^{-1}\,s^{-1}}$, $\tau_{\rm Ni} = 8.8\,{\rm days}$, and $\tau_{\rm Co} = 111.3\,{\rm days}$, are the heating rates and decay timescales for ^{56}Ni and ^{56}Co. The total amount of heating depends on how efficiently gamma-rays are thermalized. Gamma-ray thermalization efficiency, ϵ_{56}, can be simply modeled with the following function (*88*)

$$\epsilon_{56} = 1 - \exp[-(T_0/t)^2], \tag{S10}$$

where the characteristic gamma-ray diffusion timescale is (*89*)

$$T_0 = \left(\frac{10 C \kappa_\gamma M_{\rm ej}}{3 v^2}\right)^{1/2}, \tag{S11}$$

where $\kappa_\gamma = 0.03\,{\rm cm^2\,g^{-1}}$ is the fiducial gamma-ray opacity, $M_{\rm ej}$ is the total ejecta mass, and $C \sim 0.05$ is a structural factor that depends on the density distribution. A larger T_0 means that the gamma-rays take longer to diffuse and thus are more efficiently thermalized. The total luminosity is

$$L_{56} = \epsilon_{56} \dot{q}_{56} M_{56}, \tag{S12}$$

where M_{56} is the total ^{56}Ni mass.

In Figure S3, we compare the bolometric light curve of SSS17a to nickel curves with $M_{56} = 0.014\,M_\odot$, the nickel mass required to match the first night's luminosity. Since the total ejecta mass can be different from the nickel mass, we consider a range of $T_0 = 1 - 10\,{\rm days}$ (and in addition the least shallow curve is for $T_0 = \infty$, or complete thermalization of gamma-rays), corresponding to a range of ejecta masses from $M_{\rm ej} = 0.002 - 0.2\,M_\odot$. The lowest value is unphysical since it is smaller than M_{56}, but we include it just to demonstrate that no nickel-decay model can reproduce both the peak luminosity and subsequent evolution of SSS17a. In

Figure S3 we also plot a nickel curve with $M_{56} = 0.002\,M_\odot$ and $T_0 = 10\,\mathrm{days}$, corresponding to an ejecta mass of $\sim$0.2 $M_\odot$ for $v = 0.1c$. This curve reproduces the bolometric evolution of SSS17a between 7.5 and 18.5 days post-merger, but requires that another emission source dominates at early times. In addition, a transient powered by the radioactive decay of nickel does not naturally explain the color evolution observed in SSS17a.

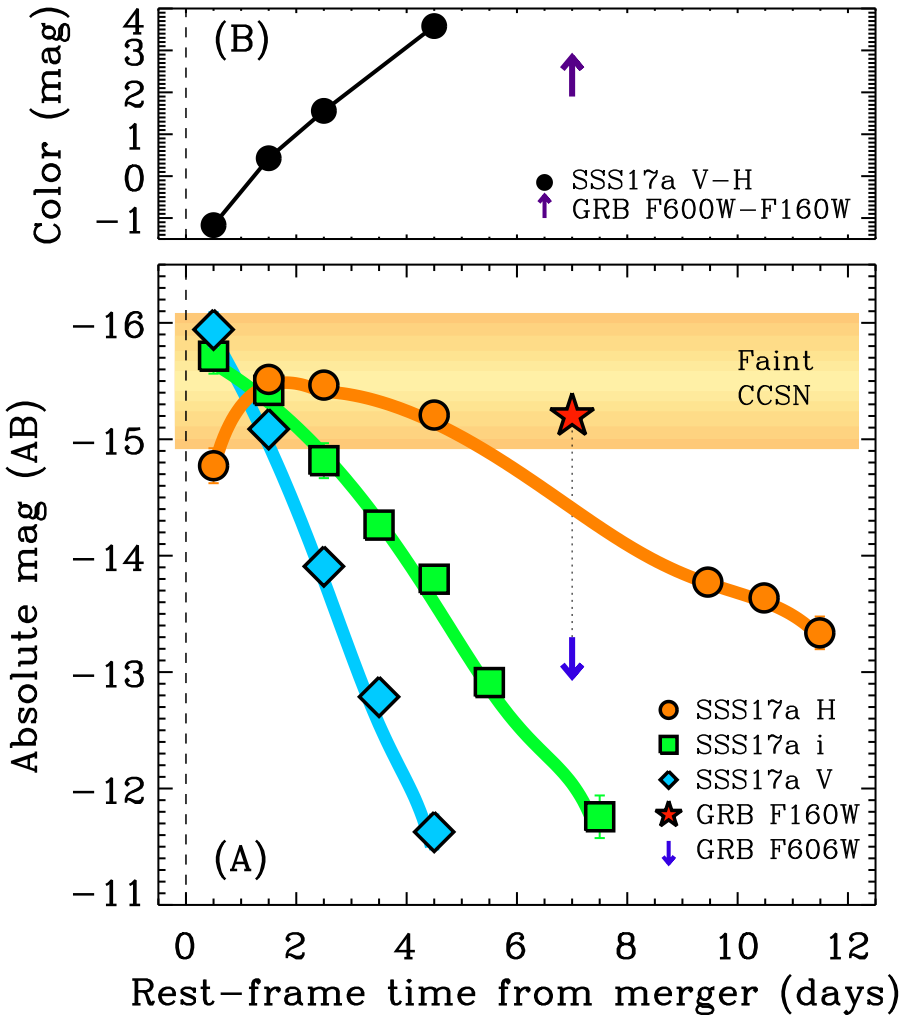

Figure S1: **Absolute magnitude light curves and $V-H$ color curves of SSS17a and the tentative kilonova associated with GRB130603B.** Vertical dashed lines indicate the time of the merger. **(A):** Absolute magnitude light curves of SSS17a in the *H*, *i*, and *V*-bands (orange circles, green squares and cyan diamonds, respectively). SSS17a reaches similar peak absolute magnitudes to faint core-collapse SNe (shaded band). Also shown are observations of the tentative kilonova associated with GRB130603B from (*23, 24*). These data correspond to roughly rest-frame *H*-band (red star) and *V*-band (blue arrow; upper limit). At $+7$ rest frame days, GRB130603B has a higher near-IR luminosity than SSS17a. **(B):** $V-H$ color. SSS17a undergoes rapid reddening in the first five days post merger. A lower limit on the color of GRB130603B is indicated by the purple arrow.

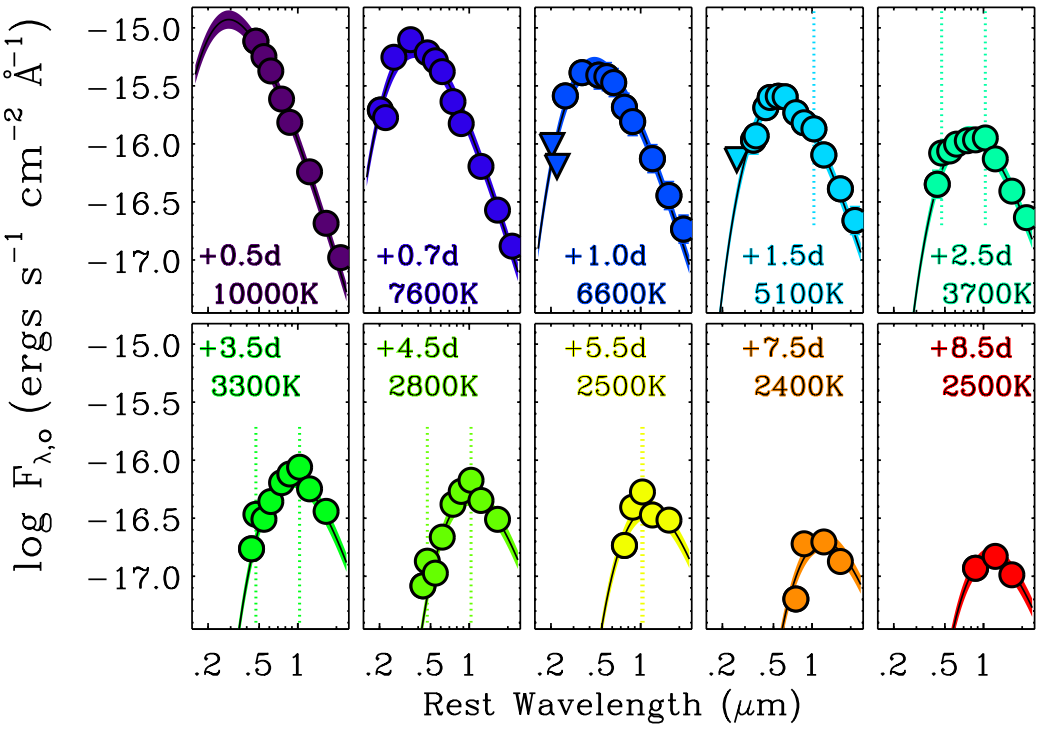

Figure S2: **Evolution of the spectral energy distribution of SSS17a, shown separately for each epoch.** Flux units are the same as in Figure 3. Detections as plotted as circles and upper limits as downward pointing triangles. Solid lines represent best-fitting blackbody model distributions. SSS17a underwent a rapid cooling in the first 48 hours post-merger. At later times the best-fit color temperature asymptotically approaches ∼2500 K.

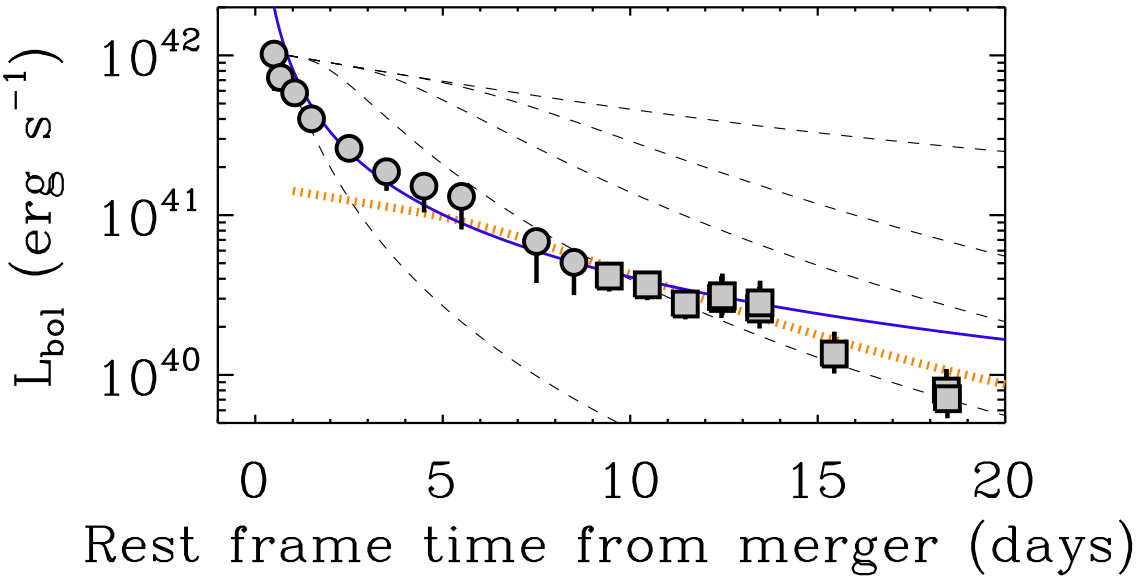

Figure S3: **Radioactive nickel and r-process heating in comparison to the bolometric light curve of SSS17a.** Data is the same as in Figure 4A. Thin black dashed lines are the heating rate from ^{56}Ni with varying levels of gamma-ray leakage with $T_0 = \infty, 10, 6, 3$, and 1 day (from top to bottom). None of these curves have the correct shape to match SSS17a. In comparison, the r-process heating (blue solid curve) better matches the data at least out to $\sim$13 days. A nickel curve with a total nickel mass of 0.002 $M_\odot$ and total ejecta mass of $\sim$0.2 $M_\odot$ (orange dotted line) can reproduce the bolometric evolution from day 7.5 to 18.5 if another emission source dominates at early times, but does not naturally explain the late-time color evolution observed for SSS17a.

Table S1: **UV to near-IR photometry of SSS17a.** Columns include the Julian Date of the observations (JD), rest frame days since the LVC trigger (phase), the broad-band filter of the observation, the observed magnitude of SSS17a (m_{obs}), and the telescope/instrument on which the observation was acquired. All magnitudes are on the AB scale and have not been corrected for foreground Milky Way reddening. Magnitude errors are given in parenthesis next to the observed magnitude and upper limits are designated with the symbol, ">". Measurements derived from performing synthetic photometry on flux calibrated spectra are designated with a "-s" in the facility/instrument column. This table is also provided in machine readable form.

JD	Phase (day)	Filter	m_{obs} (σ) (AB mag)	Facility/Instrument
2457983.6690	0.67	*uvw2*	21.11 (0.22)	Swift-UVOT
2457984.0730	1.07	*uvw2*	$>$ 21.87	Swift-UVOT
2457984.5330	1.53	*uvw2*	$>$ 21.84	Swift-UVOT
2457985.0640	2.06	*uvw2*	$>$ 22.49	Swift-UVOT
2457985.3200	2.32	*uvw2*	$>$ 22.61	Swift-UVOT
2457985.6520	2.65	*uvw2*	$>$ 22.45	Swift-UVOT
2457985.8620	2.86	*uvw2*	$>$ 23.13	Swift-UVOT
2457986.5820	3.58	*uvw2*	$>$ 22.14	Swift-UVOT
2457983.6520	0.65	*uvm2*	21.13 (0.22)	Swift-UVOT
2457984.0640	1.06	*uvm2*	$>$ 22.18	Swift-UVOT
2457984.5150	1.51	*uvm2*	$>$ 22.34	Swift-UVOT
2457985.0680	2.07	*uvm2*	$>$ 22.16	Swift-UVOT
2457985.4640	2.46	*uvm2*	$>$ 20.49	Swift-UVOT
2457985.6630	2.66	*uvm2*	$>$ 22.50	Swift-UVOT
2457985.9290	2.93	*uvm2*	$>$ 23.07	Swift-UVOT
2457986.5930	3.59	*uvm2*	$>$ 22.91	Swift-UVOT
2457983.6610	0.66	*uvw1*	19.33 (0.10)	Swift-UVOT
2457984.0680	1.07	*uvw1*	20.20 (0.22)	Swift-UVOT
2457984.5240	1.52	*uvw1*	$>$ 21.54	Swift-UVOT
2457985.0720	2.07	*uvw1*	$>$ 21.73	Swift-UVOT
2457985.2730	2.27	*uvw1*	$>$ 21.67	Swift-UVOT
2457985.6440	2.64	*uvw1*	$>$ 21.36	Swift-UVOT
2457985.8540	2.85	*uvw1*	$>$ 22.06	Swift-UVOT
2457986.5750	3.58	*uvw1*	$>$ 21.85	Swift-UVOT
2457983.6670	0.67	*u*	18.16 (0.07)	Swift-UVOT
2457984.0100	1.01	*u*	18.87 (0.15)	Swift-UVOT
2457984.0720	1.07	*u*	19.00 (0.15)	Swift-UVOT
2457984.5300	1.53	*u*	20.32 (0.30)	Swift-UVOT
2457985.0600	2.06	*u*	$>$ 21.46	Swift-UVOT
2457985.3160	2.32	*u*	20.63 (0.32)	Swift-UVOT

2457985.6480	2.65	*u*	> 20.55	Swift-UVOT
2457985.8580	2.86	*u*	> 21.30	Swift-UVOT
2457986.5780	3.58	*u*	> 20.94	Swift-UVOT
2457984.5481	1.55	*U*	20.11 (0.23)	NTT/EFOSC2
2457984.5520	1.55	*U*	20.21 (0.28)	NTT/EFOSC2
2457984.5559	1.56	*U*	20.10 (0.28)	NTT/EFOSC2
2457985.5537	2.55	*U*	> 20.19	NTT/EFOSC2
2457986.5569	3.56	*U*	> 20.49	NTT/EFOSC2
2457984.4829	1.48	*B*	19.04 (0.06)	Magellan/LDSS
2457984.4843	1.48	*B*	19.04 (0.07)	Magellan/LDSS
2457984.5342	1.53	*B*	19.07 (0.04)	Swope
2457986.4951	3.50	*B*	21.72 (0.13)	Swope
2457987.5217	4.52	*B*	22.52 (0.14)	Magellan/LDSS
2457990.5302	7.53	*B*	23.85 (0.31)	Magellan/LDSS
2457983.5057	0.51	*g*	17.41 (0.02)	Magellan/LDSS
2457983.5106	0.51	*g*	17.41 (0.04)	Magellan/LDSS
2457983.5141	0.51	*g*	17.39 (0.02)	Magellan/LDSS
2457984.4814	1.48	*g*	18.61 (0.03)	Magellan/LDSS
2457984.4875	1.49	*g*	18.66 (0.03)	Magellan/LDSS
2457984.5548	1.55	*g*	18.49 (0.12)	Swope
2457986.5013	3.50	*g*	20.77 (0.05)	Swope
2457987.5044	4.50	*g*	21.75 (0.10)	Swope
2457987.5192	4.52	*g*	21.78 (0.06)	Magellan/LDSS
2457989.7347	6.73	*g*	> 22.20	Keck/LRIS
2457990.5361	7.54	*g*	> 22.58	Magellan/LDSS
2457991.5340	8.53	*g*	> 22.64	Magellan/LDSS
2457983.5000	0.50	*V*	17.35 (0.02)	Magellna/LDSS-s
2457984.4640	1.46	*V*	18.22 (0.08)	NTT/EFOSC2
2457984.4687	1.47	*V*	18.16 (0.05)	NTT/EFOSC2
2457984.4701	1.47	*V*	18.13 (0.08)	NTT/EFOSC2
2457984.4948	1.49	*V*	18.22 (0.04)	Swope
2457984.5105	1.51	*V*	18.14 (0.04)	NTT/EFOSC2
2457984.5118	1.51	*V*	18.16 (0.06)	NTT/EFOSC2
2457984.5129	1.51	*V*	18.18 (0.04)	NTT/EFOSC2
2457984.5461	1.55	*V*	18.25 (0.06)	NTT/EFOSC2
2457984.5471	1.55	*V*	18.18 (0.10)	NTT/EFOSC2
2457985.4714	2.47	*V*	19.40 (0.11)	NTT/EFOSC2
2457985.5000	2.50	*V*	19.51 (0.08)	Magellan/IMACS-s
2457985.5164	2.52	*V*	19.53 (0.12)	NTT/EFOSC2
2457985.5537	2.55	*V*	19.59 (0.20)	NTT/EFOSC2
2457986.4687	3.47	*V*	20.54 (0.20)	NTT/EFOSC2

2457986.4893	3.49	*V*	20.52 (0.12)	Swope
2457986.5156	3.52	*V*	20.55 (0.15)	NTT/EFOSC2
2457986.5531	3.55	*V*	20.68 (0.31)	NTT/EFOSC2
2457987.5000	4.50	*V*	21.85 (0.22)	Magellan/LDSS-s
2457983.5000	0.50	*r*	17.33 (0.02)	Magellan/LDSS-s
2457984.4806	1.48	*r*	17.91 (0.03)	Magellan/LDSS
2457984.5472	1.55	*r*	17.98 (0.02)	Swope
2457985.5094	2.51	*r*	18.93 (0.02)	Magellan/IMACS
2457986.5076	3.51	*r*	19.82 (0.09)	Swope
2457987.4965	4.50	*r*	20.58 (0.12)	Swope
2457988.4645	5.46	*r*	> 19.84	Magellan/IMACS
2457983.4814	0.48	*i*	17.48 (0.02)	Swope
2457984.4798	1.48	*i*	17.77 (0.03)	Magellan/LDSS
2457984.5438	1.54	*i*	17.80 (0.02)	Swope
2457985.5000	2.50	*i*	18.36 (0.02)	Magellan/IMACS-s
2457986.5046	3.50	*i*	18.92 (0.05)	Swope
2457987.4885	4.49	*i*	19.39 (0.04)	Swope
2457988.5020	5.50	*i*	20.27 (0.12)	Swope
2457990.4897	7.49	*i*	21.42 (0.18)	Swope
2457989.7344	6.73	*I*	20.83 (0.09)	Keck/LRIS
2457983.5000	0.50	*z*	17.67 (0.03)	Magellan/LDSS-s
2457984.4768	1.48	*z*	17.62 (0.06)	Magellan/LDSS
2457984.4784	1.48	*z*	17.61 (0.06)	Magellan/LDSS
2457984.4790	1.48	*z*	17.61 (0.06)	Magellan/LDSS
2457986.5000	3.50	*z*	18.38 (0.05)	Magellan/LDSS-s
2457988.4714	5.47	*z*	19.08 (0.12)	Magellan/LDSS
2457990.4698	7.47	*z*	19.87 (0.07)	Magellan/LDSS
2457991.4720	8.47	*z*	20.40 (0.07)	Magellan/LDSS
2457995.5185	12.52	*z*	> 22.48	Magellan/IMACS
2457984.5022	1.50	*J1*	17.32 (0.01)	Magellan/FourStar
2457985.4801	2.48	*J1*	17.52 (0.01)	Magellan/FourStar
2457987.4705	4.47	*Y*	18.08 (0.02)	du Pont/RetroCam
2457988.5000	5.50	*Y*	18.33 (0.10)	du Pont/RetroCam
2457995.4600	12.46	*J1*	> 21.31	Magellan/FourStar
2457983.5000	0.50	*J*	17.83 (0.15)	Magellan/FourStar
2457984.4813	1.48	*J*	17.47 (0.01)	Magellan/FourStar
2457985.4625	2.46	*J*	17.55 (0.01)	Magellan/FourStar
2457986.4728	3.47	*J*	17.85 (0.01)	Magellan/FourStar
2457987.4986	4.50	*J*	18.10 (0.02)	du Pont/RetroCam
2457990.4903	7.49	*J*	18.99 (0.04)	du Pont/RetroCam
2457991.5000	8.50	*J*	19.30 (0.10)	du Pont/RetroCam

2457995.4600	12.46	J	> 20.65	Magellan/FourStar
2457996.5030	13.50	J	> 21.16	Magellan/FourStar
2457983.4902	0.49	H	18.26 (0.15)	Magellan/FourStar
2457984.4902	1.49	H	17.52 (0.01)	Magellan/FourStar
2457985.4714	2.47	H	17.57 (0.01)	Magellan/FourStar
2457987.4825	4.48	H	17.83 (0.02)	du Pont/RetroCam
2457988.5000	5.50	H	17.84 (0.20)	du Pont/RetroCam
2457992.4696	9.47	H	19.21 (0.05)	du Pont/RetroCam
2457993.4838	10.48	H	19.34 (0.09)	du Pont/RetroCam
2457994.4970	11.50	H	19.64 (0.14)	NTT/SOFI
2457995.4600	12.46	H	> 20.30	Magellan/FourStar
2457996.4620	13.46	H	> 20.50	Magellan/FourStar
2457998.4697	15.47	H	> 20.50	Magellan/FourStar
2457983.5300	0.53	K_s	18.41 (0.15)	Magellan/FourStar
2457984.4810	1.48	K_s	17.61 (0.04)	Magellan/FourStar
2457985.4620	2.46	K_s	17.55 (0.06)	Magellan/FourStar
2457995.4620	12.46	K_s	19.36 (0.09)	Magellan/FourStar
2457995.4850	12.48	K_s	19.32 (0.09)	NTT/SOFI
2457996.4780	13.48	K_s	19.52 (0.09)	Magellan/FourStar
2457996.4900	13.49	K_s	19.43 (0.09)	NTT/SOFI
2457998.4697	15.47	K_s	20.23 (0.10)	Magellan/FourStar
2458001.4600	18.46	K_s	20.81 (0.13)	Magellan/FourStar
2458001.4900	18.49	K_s	20.93 (0.17)	Magellan/FourStar

Table S2: **Photometric Properties of SSS17a.** Columns include the observed broad-band filter, the peak observed apparent magnitude ($m_{obs,max}$), the peak observed absolute magnitude ($M_{obs,max}$), the observed rise time (t_{rise}), the decline rate measured in the first 5 days post-observed-maximum, the time for the light curve to decline by half of its peak flux ($t_{1/2,decline}$), and the number of magnitudes the light curve declines in the first five days post-maximum (Δm_5). Times are given in rest-frame days since LVC trigger. Uncertainties (1σ) are given in parentheses next to each measurement. Upper and lower limits are designated with the symbols "<" and ">", respectively. All magnitude measurements are listed on the AB scale. Apparent magnitudes have been corrected for Milky Way extinction. Errors in absolute magnitude account for an uncertainty in the distance to NGC 4993 of 3 Mpc based on the range of distances listed in the NASA/IPAC Extragalactic Database.

Filter	$m_{obs,max}$ (mag)	$M_{obs,max}$ (mag)	t_{rise} (day)	Decline Rate (mag day^{-1})	$t_{1/2,decline}$ (day)	Δm_5 (mag)
K_s	17.51 (0.05)	-15.46 (0.17)	2.5 (0.5)		3.11 (0.15)	0.85 (0.06)
H	17.46 (0.02)	-15.51 (0.16)	1.5 (0.5)	0.10 (0.01)	3.66 (0.95)	0.88 (0.02)
J	17.37 (0.01)	-15.60 (0.16)	1.5 (0.5)	0.23 (0.01)	3.41 (0.06)	1.23 (0.03)
Y	17.20 (0.01)	-15.78 (0.16)	<1.5	0.25 (0.01)	2.98 (0.09)	1.26 (0.18)
z	17.45 (0.06)	-15.52 (0.17)	1.0 (0.5)	0.38 (0.01)	2.00 (0.50)	1.86 (0.11)
i	17.26 (0.15)	-15.71 (0.23)	<0.5	0.57 (0.01)	1.78 (0.31)	2.80 (0.19)
r	17.00 (0.14)	-15.97 (0.21)	<0.5	0.95 (0.02)	1.12 (0.15)	4.06 (0.30)
V	16.93 (0.15)	-16.04 (0.23)	<0.5	1.13 (0.04)	0.79 (0.12)	5.58 (0.37)
g	17.01 (0.15)	-15.96 (0.16)	<0.5	1.14 (0.02)	0.62 (0.02)	5.39 (0.13)
B	18.61 (0.06)	-14.35 (0.17)	<1.5	1.37 (0.06)	0.51 (0.05)	5.77 (0.35)
u	17.71 (0.07)	-15.26 (0.17)	<0.67	2.58 (0.31)	0.30 (0.05)	
$w1$	18.74 (0.09)	-14.23 (0.18)	<0.67	2.65 (0.74)	0.28 (0.07)	
$m2$	20.28 (0.22)	-12.69 (0.27)	<0.67	> 3.2		
$w2$	20.32 (0.22)	-12.65 (0.27)	<0.67	> 2.3		

References

1. LIGO Scientific Collaboration and Virgo Collaboration, Binary black hole mergers in the first advanced LIGO observing run. *Phys. Rev. X* **6**, 041015 (2016). doi:10.1103/PhysRevX.6.041015

2. LIGO Scientific Collaboration and Virgo Collaboration, Observation of gravitational waves from a binary black hole merger. *Phys. Rev. Lett.* **116**, 061102 (2016). doi:10.1103/PhysRevLett.116.061102 Medline

3. S. A. Hughes, D. E. Holz, Cosmology with coalescing massive black holes. *Class. Quantum Gravity* **20**, S65–S72 (2003). doi:10.1088/0264-9381/20/10/308

4. D. E. Holz, S. A. Hughes, Using gravitational-wave standard sirens. *Astrophys. J.* **629**, 15–22 (2005). doi:10.1086/431341

5. S. Nissanke, D. E. Holz, N. Dalal, S. A. Hughes, J. L. Sievers, C. M. Hirata, Determining the Hubble constant from gravitational wave observations of merging compact binaries. arXiv:astro-ph/1307.2638 [astro-ph.CO] (10 July 2013).

6. E. S. Phinney, Astro2010: The Astronomy and Astrophysics Decadal Survey, Science White Papers. arXiv:astro-ph/0903.0098 [astro-ph.CO] (28 February 2009).

7. I. Mandel, R. O'Shaughnessy, Compact binary coalescences in the band of ground-based gravitational-wave detectors. *Class. Quantum Gravity* **27**, 114007 (2010). doi:10.1088/0264-9381/27/11/114007

8. B. Paczynski, Gamma-ray bursters at cosmological distances. *Astrophys. J.* **308**, L43 (1986). doi:10.1086/184740

9. D. Eichler, M. Livio, T. Piran, D. N. Schramm, Nucleosynthesis, neutrino bursts and γ-rays from coalescing neutron stars. *Nature* **340**, 126–128 (1989). doi:10.1038/340126a0

10. L. Z. Kelley, I. Mandel, E. Ramirez-Ruiz, Electromagnetic transients as triggers in searches for gravitational waves from compact binary mergers. *Phys. Rev. D Part. Fields Gravit. Cosmol.* **87**, 123004 (2013). doi:10.1103/PhysRevD.87.123004

11. W. Fong, E. Berger, R. Margutti, B. A. Zauderer, A decade of short-duration gamma-ray burst broadband afterglows: energetics, circumburst densities, and jet opening angles. *Astrophys. J.* **815**, 102 (2015). doi:10.1088/0004-637X/815/2/102

12. L.-X. Li, B. Paczy, Transient events from neutron star mergers. *Astrophys. J.* **507**, L59–L62 (1998). doi:10.1086/311680

13. S. R. Kulkarni, Modeling supernova-like explosions associated with gamma-ray bursts with short durations. arXiv:astro-ph/0510256 [astro-ph.CO] (10 October 2005).

14. B. D. Metzger, G. Martínez-Pinedo, S. Darbha, E. Quataert, A. Arcones, D. Kasen, R. Thomas, P. Nugent, I. V. Panov, N. T. Zinner, Electromagnetic counterparts of compact object mergers powered by the radioactive decay of r-process nuclei. *Mon. Not. R. Astron. Soc.* **406**, 2650–2662 (2010). doi:10.1111/j.1365-2966.2010.16864.x

15. L. F. Roberts, D. Kasen, W. H. Lee, E. Ramirez-Ruiz, Electromagnetic transients powered by nuclear decay in the tidal tails of coalescing compact binaries. *Astrophys. J.* **736**, L21 (2011). doi:10.1088/2041-8205/736/1/L21

16. T. Piran, E. Nakar, S. Rosswog, The electromagnetic signals of compact binary mergers. *Mon. Not. R. Astron. Soc.* **430**, 2121–2136 (2013). doi:10.1093/mnras/stt037

17. B. D. Metzger, Kilonovae. *Living Rev. Relativ.* **20**, 3 (2017). doi:10.1007/s41114-017-0006-z Medline

18. S. Shen, R. J. Cooke, E. Ramirez-Ruiz, P. Madau, L. Mayer, J. Guedes, The history of r-process enrichment in the Milky Way. *Astrophys. J.* **807**, 115 (2015). doi:10.1088/0004-637X/807/2/115

19. E. M. Burbidge, G. R. Burbidge, W. A. Fowler, F. Hoyle, Synthesis of the elements in stars. *Rev. Mod. Phys.* **29**, 547–650 (1957). doi:10.1103/RevModPhys.29.547

20. A. G. W. Cameron, Nuclear reactions in stars and nucleogenesis. *Publ. Astron. Soc. Pac.* **69**, 201 (1957). doi:10.1086/127051

21. Y.-Z. Qian, G. J. Wasserburg, Where, oh where has the r-process gone? *Phys. Rep.* **442**, 237–268 (2007). doi:10.1016/j.physrep.2007.02.006

22. M. Arnould, S. Goriely, K. Takahashi, The r-process of stellar nucleosynthesis: Astrophysics and nuclear physics achievements and mysteries. *Phys. Rep.* **450**, 97–213 (2007). doi:10.1016/j.physrep.2007.06.002

23. N. R. Tanvir, A. J. Levan, A. S. Fruchter, J. Hjorth, R. A. Hounsell, K. Wiersema, R. L. Tunnicliffe, A 'kilonova' associated with the short-duration γ-ray burst GRB 130603B. *Nature* **500**, 547–549 (2013). doi:10.1038/nature12505 Medline

24. E. Berger, W. Fong, R. Chornock, An r-process kilonova associated with the short-hard GRB 130603B. *Astrophys. J.* **774**, L23 (2013). doi:10.1088/2041-8205/774/2/L23

25. LIGO/Virgo Collaboration, *GRB Coordinates Network* **21509** (2017).

26. LIGO/Virgo Collaboration, *GRB Coordinates Network* **21513** (2017).

27. B. P. Abbott *et al.*, *Phys. Rev. Lett.* 10.1103/PhysRevLett.119.161101 (2017). 10.1103/PhysRevLett.119.161101

28. One-Meter Two-Hemisphere (1M2H) Collaboration, *GRB Coordinates Network* **21529** (2017).

29. D. A. Coulter, R. J. Foley, C. D. Kilpatrick, M. R. Drout, A. L. Piro, B. J. Shappee, M. R. Siebert, J. D. Simon, N. Ulloa, D. Kasen, B. F. Madore, A. Murguia-Berthier, Y.-C. Pan, J. X. Prochaska, E. Ramirez-Ruiz, A. Rest, C. Rojas-Bravo, Swope Supernova Survey 2017a (SSS17a), the optical counterpart to a gravitational wave source. *Science* 10.1126/science.aap9811 (2017). doi:10.1126/science.aap9811

30. J. D. Simon *et al., GRB Coordinates Network* **21551** (2017).

31. M. R. Drout *et al., GRB Coordinates Network* **21547** (2017).

32. B. J. Shappee, J. D. Simon, M. R. Drout, A. L. Piro, N. Morrell, J. L. Prieto, D. Kasen, T. W.-S. Holoien, J. A. Kollmeier, D. D. Kelson, D. A. Coulter, R. J. Foley, C. D. Kilpatrick, M. R. Siebert, B. F. Madore, A. Murguia-Berthier, Y.-C. Pan, J. X. Prochaska, E. Ramirez-Ruiz, A. Rest, C. Adams, K. Alatalo, E. Bañados, J. Baughman, R. A. Bernstein, T. Bitsakis, K. Boutsia, J. R. Bravo, F. Di Mille, C. R. Higgs, A. P. Ji, G. Maravelias, J. L. Marshall, V. M. Placco, G. Prieto, Z. Wan, Early spectra of the

gravitational wave source GW170817: Evolution of a neutron star merger. *Science* 10.1126/science.aaq0186 (2017). 10.1126/science.aaq0186

33. Materials and methods are available as supplementary materials.

34. M. R. Siebert *et al*., *Astrophys. J.* **848**, aa905e (2017). 10.3847/2041-8213/aa905e

35. W. D. Arnett, Type I supernovae. I - Analytic solutions for the early part of the light curve. *Astrophys. J.* **253**, 785 (1982). doi:10.1086/159681

36. D. Kasen, N. R. Badnell, J. Barnes, Opacities and spectra of the r-process ejecta from neutron star mergers. *Astrophys. J.* **774**, 25 (2013). doi:10.1088/0004-637X/774/1/25

37. A. Perego, S. Rosswog, R. M. Cabezon, O. Korobkin, R. Kappeli, A. Arcones, M. Liebendorfer, Neutrino-driven winds from neutron star merger remnants. *Mon. Not. R. Astron. Soc.* **443**, 3134–3156 (2014). doi:10.1093/mnras/stu1352

38. R. Fernández, B. D. Metzger, Electromagnetic signatures of neutron star mergers in the advanced LIGO era. *Annu. Rev. Nucl. Part. Sci.* **66**, 23–45 (2016). doi:10.1146/annurev-nucl-102115-044819

39. K. Hotokezaka, K. Kiuchi, K. Kyutoku, H. Okawa, Y. Sekiguchi, M. Shibata, K. Taniguchi, Mass ejection from the merger of binary neutron stars. *Phys. Rev. D Part. Fields Gravit. Cosmol.* **87**, 024001 (2013). doi:10.1103/PhysRevD.87.024001

40. R. Fernández, D. Kasen, B. D. Metzger, E. Quataert, Outflows from accretion discs formed in neutron star mergers: Effect of black hole spin. *Mon. Not. R. Astron. Soc.* **446**, 750–758 (2015). doi:10.1093/mnras/stu2112

41. S. Wanajo, Y. Sekiguchi, N. Nishimura, K. Kiuchi, K. Kyutoku, M. Shibata, Production of all the *r* -process nuclides in the dynamical ejecta of neutron star mergers. *Astrophys. J.* **789**, L39 (2014). doi:10.1088/2041-8205/789/2/L39

42. L. Bovard, D. Martin, F. Guercilena, A. Arcones, L. Rezzolla, O. Korobkin, On r-process nucleosynthesis from matter ejected in binary neutron starmergers. arXiv:astro-ph/1709/09630 [gr-qc] (27 September 2017).

43. D. Kasen, R. Fernández, B. D. Metzger, Kilonova light curves from the disc wind outflows of compact object mergers. *Mon. Not. R. Astron. Soc.* **450**, 1777–1786 (2015). doi:10.1093/mnras/stv721

44. C. D. Kilpatrick, R. J. Foley, D. Kasen, A. Murguia-Berthier, E. Ramirez-Ruiz, D. A. Coulter, M. R. Drout, A. L. Piro, B. J. Shappee, K. Boutsia, C. Contreras, F. Di Mille, B. F. Madore, N. Morrell, Y.-C. Pan, J. X. Prochaska, A. Rest, C. Rojas-Bravo, M. R. Siebert, J. D. Simon, N. Ulloa, Electromagnetic evidence that SSS17a is the result of a binary neutron star merger. *Science* 10.1126/science.aaq0073 (2017). 10.1126/science.aaq0073

45. A. Elmhamdi, I. J. Danziger, N. Chugai, A. Pastorello, M. Turatto, E. Cappellaro, G. Altavilla, S. Benetti, F. Patat, M. Salvo, Photometry and spectroscopy of the type IIP SN 1999em from outburst to dust formation. *Mon. Not. R. Astron. Soc.* **338**, 939–956 (2003). doi:10.1046/j.1365-8711.2003.06150.x

46. B. D. Metzger, A. L. Piro, Optical and x-ray emission from stable millisecond magnetars formed from the merger of binary neutron stars. *Mon. Not. R. Astron. Soc.* **439**, 3916–3930 (2014). doi:10.1093/mnras/stu247

47. B. D. Metzger, A. L. Piro, E. Quataert, Neutron-rich freeze-out in viscously spreading accretion discs formed from compact object mergers. *Mon. Not. R. Astron. Soc.* **396**, 304–314 (2009). doi:10.1111/j.1365-2966.2008.14380.x

48. O. Gottlieb, E. Nakar, T. Piran, The cocoon emission: An electromagnetic counterpart to gravitational waves from neutron star mergers. arXiv:astro-ph/1705.10797 [astro-ph.HE] (30 May 2017).

49. F. Kappeler, H. Beer, K. Wisshak, s-process nucleosynthesis-nuclear physics and the classical model. *Rep. Prog. Phys.* **52**, 945–1013 (1989). doi:10.1088/0034-4885/52/8/002

50. Y. Qian, Supernovae versus neutron star mergers as the major r-process sources. *Astrophys. J.* **534**, L67–L70 (2000). doi:10.1086/312659 Medline

51. LIGO Scientific Collaboration; Virgo Collaboration, Prospects for observing and localizing gravitational-wave transients with advanced LIGO and advanced Virgo. *Living Rev. Relativ.* **19**, 1 (2016). doi:10.1007/lrr-2016-1 Medline

52. O. Yaron, A. Gal-Yam, WISeREP—An interactive supernova data repository. *Publ. Astron. Soc. Pac.* **124**, 668–681 (2012). doi:10.1086/666656

53. J. Guillochon, J. Parrent, L. Z. Kelley, R. Margutti, An open catalog for supernova data. *Astrophys. J.* **835**, 64 (2017). doi:10.3847/1538-4357/835/1/64

54. A. Rest, C. Stubbs, A. C. Becker, G. A. Miknaitis, A. Miceli, R. Covarrubias, S. L. Hawley, R. C. Smith, N. B. Suntzeff, K. Olsen, J. L. Prieto, R. Hiriart, D. L. Welch, K. H. Cook, S. Nikolaev, M. Huber, G. Prochtor, A. Clocchiatti, D. Minniti, A. Garg, P. Challis, S. C. Keller, B. P. Schmidt, Testing LMC microlensing scenarios: The discrimination power of the SuperMACHO Microlensing Survey. *Astrophys. J.* **634**, 1103–1115 (2005). doi:10.1086/497060

55. A. Rest, D. Scolnic, R. J. Foley, M. E. Huber, R. Chornock, G. Narayan, J. L. Tonry, E. Berger, A. M. Soderberg, C. W. Stubbs, A. Riess, R. P. Kirshner, S. J. Smartt, E. Schlafly, S. Rodney, M. T. Botticella, D. Brout, P. Challis, I. Czekala, M. Drout, M. J. Hudson, R. Kotak, C. Leibler, R. Lunnan, G. H. Marion, M. McCrum, D. Milisavljevic, A. Pastorello, N. E. Sanders, K. Smith, E. Stafford, D. Thilker, S. Valenti, W. M. Wood-Vasey, Z. Zheng, W. S. Burgett, K. C. Chambers, L. Denneau, P. W. Draper, H. Flewelling, K. W. Hodapp, N. Kaiser, R.-P. Kudritzki, E. A. Magnier, N. Metcalfe, P. A. Price, W. Sweeney, R. Wainscoat, C. Waters, Cosmological constraints from measurements of type Ia supernovae discovered during the first 1.5 yr of the Pan-STARRS1 Survey. *Astrophys. J.* **795**, 44 (2014). doi:10.1088/0004-637X/795/1/44

56. D. Scolnic, S. Casertano, A. Riess, A. Rest, E. Schlafly, R. J. Foley, D. Finkbeiner, C. Tang, W. S. Burgett, K. C. Chambers, P. W. Draper, H. Flewelling, K. W. Hodapp, M. E. Huber, N. Kaiser, R. P. Kudritzki, E. A. Magnier, N. Metcalfe, C. W. Stubbs, SUPERCAL: Cross-calibration of multiple photometric systems to improve cosmological measurements with type Ia supernovae. *Astrophys. J.* **815**, 117 (2015). doi:10.1088/0004-637X/815/2/117

57. A. Dressler, T. Hare, B. C. Bigelow, D. J. Osip, *Society of Photo-Optical Instrumentation Engineers (SPIE) Conference Series* (2006), vol. 6269 of *Proc.SPIE*, p. 62690F.

58. IRAF is distributed by the National Optical Astronomy Observatory, which is operated by the Association of Universities for Research in Astronomy (AURA) under a cooperative agreement with the National Science Foundation.

59. K. C. Chambers *et al*., The Pan-STARRS1 surveys. arXiv:astro-ph/1612.05560 [astro-ph.IM] (16 December 2016).

60. P. B. Stetson, DAOPHOT - A computer program for crowded-field stellar photometry. *Publ. Astron. Soc. Pac.* **99**, 191 (1987). doi:10.1086/131977

61. H. A. Flewelling *et al*., The Pan-STARRS1 database and data products. arXiv:astro-ph/1612.05243 [astro-ph.IM] (15 December 2016).

62. S. E. Persson, D. C. Murphy, S. Smee, C. Birk, A. J. Monson, A. Uomoto, E. Koch, S. Shectman, R. Barkhouser, J. Orndorff, R. Hammond, A. Harding, G. Scharfstein, D. Kelson, J. Marshall, P. J. McCarthy, FourStar: The Near-Infrared Imager for the 6.5 m Baade Telescope at Las Campanas Observatory. *Publ. Astron. Soc. Pac.* **125**, 654–682 (2013). doi:10.1086/671164

63. M. F. Skrutskie, R. M. Cutri, R. Stiening, M. D. Weinberg, S. Schneider, J. M. Carpenter, C. Beichman, R. Capps, T. Chester, J. Elias, J. Huchra, J. Liebert, C. Lonsdale, D. G. Monet, S. Price, P. Seitzer, T. Jarrett, J. D. Kirkpatrick, J. E. Gizis, E. Howard, T. Evans, J. Fowler, L. Fullmer, R. Hurt, R. Light, E. L. Kopan, K. A. Marsh, H. L. McCallon, R. Tam, S. Van Dyk, S. Wheelock, The Two Micron All Sky Survey (2MASS). *Astron. J.* **131**, 1163–1183 (2006). doi:10.1086/498708

64. M. R. Blanton, D. J. Schlegel, M. A. Strauss, J. Brinkmann, D. Finkbeiner, M. Fukugita, J. E. Gunn, D. W. Hogg, Ž. Ivezić, G. R. Knapp, R. H. Lupton, J. A. Munn, D. P. Schneider, M. Tegmark, I. Zehavi, New York University Value-Added Galaxy Catalog: A galaxy catalog based on new public surveys. *Astron. J.* **129**, 2562–2578 (2005). doi:10.1086/429803

65. K. Krisciunas *et al*., The Carnegie Supernova Project I: Third photometry data release of low-redshift type Ia supernovae and other white dwarf explosions. arXiv:astro-ph/1709.05146 [astro-ph.IM] (15 September 2017).

66. Swift Team, *GRB Coordinates Network* **21550** (2017).

67. Swift Team, *GRB Coordinates Network* **21572** (2017).

68. T. S. Poole, A. A. Breeveld, M. J. Page, W. Landsman, S. T. Holland, P. Roming, N. P. M. Kuin, P. J. Brown, C. Gronwall, S. Hunsberger, S. Koch, K. O. Mason, P. Schady, D. V. Berk, A. J. Blustin, P. Boyd, P. Broos, M. Carter, M. M. Chester, A. Cucchiara, B. Hancock, H. Huckle, S. Immler, M. Ivanushkina, T. Kennedy, F. Marshall, A. Morgan, S. B. Pandey, M. De Pasquale, P. J. Smith, M. Still, Photometric calibration of the Swift ultraviolet/optical telescope. *Mon. Not. R. Astron. Soc.* **383**, 627–645 (2008). doi:10.1111/j.1365-2966.2007.12563.x

69. A. A. Breeveld *et al*., *Mon. Not. R. Astron. Soc.* **406**, 1687 (2010).

70. S. J. Smartt, S. Valenti, M. Fraser, C. Inserra, D. R. Young, M. Sullivan, A. Pastorello, S. Benetti, A. Gal-Yam, C. Knapic, M. Molinaro, R. Smareglia, K. W. Smith, S. Taubenberger, O. Yaron, J. P. Anderson, C. Ashall, C. Balland, C. Baltay, C. Barbarino, F. E. Bauer, S. Baumont, D. Bersier, N. Blagorodnova, S. Bongard, M. T. Botticella, F. Bufano, M. Bulla, E. Cappellaro, H. Campbell, F. Cellier-Holzem, T.-W. Chen, M. J. Childress, A. Clocchiatti, C. Contreras, M. Dall'Ora, J. Danziger, T. de Jaeger, A. De Cia, M. Della Valle, M. Dennefeld, N. Elias-Rosa, N. Elman, U. Feindt, M. Fleury, E. Gall, S. Gonzalez-Gaitan, L. Galbany, A. Morales Garoffolo, L. Greggio, L. L. Guillou, S. Hachinger, E. Hadjiyska, P. E. Hage, W. Hillebrandt, S. Hodgkin, E. Y. Hsiao, P. A. James, A. Jerkstrand, T. Kangas, E. Kankare, R. Kotak, M. Kromer, H. Kuncarayakti, G. Leloudas, P. Lundqvist, J. D. Lyman, I. M. Hook, K. Maguire, I. Manulis, S. J. Margheim, S. Mattila, J. R. Maund, P. A. Mazzali, M. McCrum, R. McKinnon, M. E. Moreno-Raya, M. Nicholl, P. Nugent, R. Pain, G. Pignata, M. M. Phillips, J. Polshaw, M. L. Pumo, D. Rabinowitz, E. Reilly, C. Romero-Cañizales, R. Scalzo, B. Schmidt, S. Schulze, S. Sim, J. Sollerman, F. Taddia, L. Tartaglia, G. Terreran, L. Tomasella, M. Turatto, E. Walker, N. A. Walton, L. Wyrzykowski, F. Yuan, L. Zampieri, PESSTO: Survey description and products from the first data release by the Public ESO Spectroscopic Survey of Transient Objects. *Astron. Astrophys.* **579**, A40 (2015). doi:10.1051/0004-6361/201425237

71. B. Buzzoni *et al.*, *Messenger (Los Angel.)* **38**, 9 (1984).

72. A. Moorwood, J.-G. Cuby, C. Lidman, *Messenger (Los Angel.)* **91**, 9 (1998).

73. J. D. Lyman *et al.*, *GRB Coordinates Network* **21582** (2017).

74. J. B. Oke, J. G. Cohen, M. Carr, J. Cromer, A. Dingizian, F. H. Harris, S. Labrecque, R. Lucinio, W. Schaal, H. Epps, J. Miller, The Keck Low-Resolution Imaging Spectrometer. *Publ. Astron. Soc. Pac.* **107**, 375 (1995). doi:10.1086/133562

75. C. C. Steidel, A. E. Shapley, M. Pettini, K. L. Adelberger, D. K. Erb, N. A. Reddy, M. P. Hunt, A Survey of Star-forming Galaxies in the $1.4 \lesssim z \lesssim 2.5$ Redshift Desert: Overview. *Astrophys. J.* **604**, 534–550 (2004). doi:10.1086/381960

76. A. U. Landolt, UBVRI photometric standard stars in the magnitude range 11.5-16.0 around the celestial equator. *Astron. J.* **104**, 340 (1992). doi:10.1086/116242

77. LPipe: LRIS automated reduction pipeline; http://www.astro.caltech.edu/~dperley/programs/lpipe.html

78. A. A. Henden, M. Templeton, D. Terrell, T. C. Smith, S. Levine, D. Welch, *VizieR Online Data Catalog: II/336* (2016); http://adsabs.harvard.edu/abs/2016yCat.2336....0H

79. W. L. Freedman, B. F. Madore, B. K. Gibson, L. Ferrarese, D. D. Kelson, S. Sakai, J. R. Mould, R. C. Kennicutt Jr., H. C. Ford, J. A. Graham, J. P. Huchra, S. M. G. Hughes, G. D. Illingworth, L. M. Macri, P. B. Stetson, Final Results from the *Hubble Space Telescope* Key Project to Measure the Hubble Constant. *Astrophys. J.* **553**, 47–72 (2001). doi:10.1086/320638

80. E. F. Schlafly, D. P. Finkbeiner, Measuring reddening with Sloan Digital Sky Survey stellar spectra and recalibrating SFD. *Astrophys. J.* **737**, 103 (2011). doi:10.1088/0004-637X/737/2/103

81. J. A. Cardelli, G. C. Clayton, J. S. Mathis, The relationship between infrared, optical, and ultraviolet extinction. *Astrophys. J.* **345**, 245 (1989). doi:10.1086/167900

82. M. R. Drout, R. Chornock, A. M. Soderberg, N. E. Sanders, R. McKinnon, A. Rest, R. J. Foley, D. Milisavljevic, R. Margutti, E. Berger, M. Calkins, W. Fong, S. Gezari, M. E. Huber, E. Kankare, R. P. Kirshner, C. Leibler, R. Lunnan, S. Mattila, G. H. Marion, G. Narayan, A. G. Riess, K. C. Roth, D. Scolnic, S. J. Smartt, J. L. Tonry, W. S. Burgett, K. C. Chambers, K. W. Hodapp, R. Jedicke, N. Kaiser, E. A. Magnier, N. Metcalfe, J. S. Morgan, P. A. Price, C. Waters, Rapidly evolving and luminous transients from Pan-STARRS1. *Astrophys. J.* **794**, 23 (2014). doi:10.1088/0004-637X/794/1/23

83. P. J. Brown, A. Breeveld, P. W. A. Roming, M. Siegel, Interpreting flux from broadband photometry. *Astron. J.* **152**, 102 (2016). doi:10.3847/0004-6256/152/4/102

84. B. D. Metzger, A. L. Piro, E. Quataert, *Mon. Not. R. Astron. Soc.* **390**, 781 (2008).

85. J. Barnes, D. Kasen, M.-R. Wu, G. Martínez-Pinedo, Radioactivity and thermalization in the ejecta of compact object mergers and their impact on kilonova light curves. *Astrophys. J.* **829**, 110 (2016). doi:10.3847/0004-637X/829/2/110

86. A. Bauswein, S. Goriely, H.-T. Janka, Systematics of dynamical mass ejection, nucleosynthesis, and radioactively powered electromagnetic signals from neutron-star mergers. *Astrophys. J.* **773**, 78 (2013). doi:10.1088/0004-637X/773/1/78

87. S. Rosswog, O. Korobkin, A. Arcones, F.-K. Thielemann, T. Piran, The long-term evolution of neutron star merger remnants - I. The impact of r-process nucleosynthesis. *Mon. Not. R. Astron. Soc.* **439**, 744–756 (2014). doi:10.1093/mnras/stt2502

88. J. C. Wheeler, V. Johnson, A. Clocchiatti, Analysis of late-time light curves of Type IIb, Ib and Ic supernovae. *Mon. Not. R. Astron. Soc.* **450**, 1295–1307 (2015). doi:10.1093/mnras/stv650

89. A. Clocchiatti, J. C. Wheeler, On the light curves of stripped-envelope supernovae. *Astrophys. J.* **491**, 375–380 (1997). doi:10.1086/304961